Supplemental Information Appendix

Molecular basis for lipid recognition by the prostaglandin D_2 receptor CRTH2

Heng Liu[1#], R. N. V. Krishna Deepak[2#], Anna Shiriaeva[3,4#], Cornelius Gati[3,5], Alexander Batyuk[6], Hao Hu[7], Uwe Weierstall[7], Wei Liu[8,9], Lei Wang[1], Vadim Cherezov[3-5*], Hao Fan[2*], Cheng Zhang[1*]

Supplementary Materials & Methods

Protein expression, purification and crystallization. A modified T4 lysozyme (eT4L)(1) was inserted into the third intracellular loop (ICL3) between residues R236 and R238, along with an accidentally introduced linker (ADLGLQHR) at the N terminus of eT4L. To facilitate crystallization, the glycosylation site N25 was mutated to alanine and the C terminus was removed by inserting a human rhinovirus (3C) protease cleavage site at residue S339. To purify the protein, a Flag-tag was introduced at the N terminus followed by a tobacco etch virus (TEV) protease cleavage site, and an 8 × His-tag was attached to the C terminus. The construct was cloned into an Sf9 expression vector pFastBac1 (Thermo Fisher Scientific) for generating baculovirus. Cells were infected with the baculovirus in the presence of an antagonist, ramatroban (BAY u3405) (Cayman Chemical), at a concentration of 100 nM in the medium, then collected by centrifugation after 48h and stored at -80 °C for further use.

To purify the protein, frozen Sf9 cells were lysed by stirring in buffer containing 20 mM Tris-HCl, pH7.5, 0.2 μg/ml leupeptin, 100 μg/ml benzamidine, 2 mg/ml iodoacetamide and 1 μM ramatroban. Cell membranes were isolated by centrifugation at 25,000 g for 40 min. Then the pellet was resuspended and solubilized in buffer containing 20 mM HEPES, pH 7.5, 750 mM NaCl, 1% (w/v) n-dodecyl-b-D-maltoside (DDM, Anatrace), 0.2% (w/v) sodium cholate (Sigma), 0.1% (w/v) cholesterol hemisuccinate (CHS, Anatrace), 20% (v/v) glycerol, 0.2 μg/ml leupeptin, 100 μg/ml benzamidine, 500 unit Salt Active Nuclease (Arcticzymes), 2 mg/ml iodoacetamide and 1 μM ramatroban at 4°C for 2h. Insoluble material was separated by centrifugation at 25,000 g for 40 min. The supernatant was incubated with nickel sepharose resin (GE healthcare) plus 10 mM imidazole at 4°C overnight. The resin was washed with 5 column volume of buffer containing 20 mM HEPES, pH 7.5, 500 mM NaCl, 0.1% (w/v) DDM, 0.02% (w/v) CHS, 25 mM imidazole and 1 μM ramatroban. The protein was eluted with buffer containing 20 mM HEPES, pH 7.5, 500 mM NaCl, 0.1% (w/v) DDM, 0.02% (w/v) CHS, 400 mM imidazole and 1 μM ramatroban and loaded onto an anti-Flag M1 antibody resin (homemade) after adding 2mM $CaCl_2$. The detergent was slowly exchanged to 0.01% (w/v) lauryl maltose neopentyl glycol (MNG, Anatrace) containing 1μM 15mPGD$_2$ on the M1 antibody resin. The protein was finally eluted with buffer containing 20 mM HEPES, pH 7.5, 100 mM NaCl, 0.002% (w/v) MNG, 0.001% (w/v) CHS, 200 mg/ml Flag peptide, 5 mM EDTA and 1μM 15mPGD$_2$. To remove the N-terminal Flag-tag, the C-terminal His-tag and glycosylation, the protein was treated with TEV protease, 3C protease and PNGase F (NEB) at 4°C overnight. The protein was further purified by size-exclusion chromatography using a Superdex 200 Increase column (GE healthcare). The receptor was collected and concentrated to 30–40 mg ml^{-1} with a 100-kDa molecular weight cut-off concentrator (Millipore) for crystallization.

The protein was initially crystallized using the lipidic mesophase method (2). The protein was mixed with monoolein (Sigma) and cholesterol (Sigma) (10:1 wt/wt) using the two-syringe mixing method at a weight ratio 2:3 (protein/lipid) and at room temperature. After a clear lipidic cubic phase formed, the mesophase was dispensed onto custom-made 96-well glass sandwich plates in 10–30 nl drops overlaid with 700 nl crystallization solution using a Gryphon LCP robot (Art Robbins Instruments). Crystals appeared in 4 d at 10 °C and continued to grow to full size after 1 months. The best crystals only grew to 5 μm in the conditions containing 0.1 M sodium chloride, 0.1 M lithium sulphate, 0.1 M sodium citrate tribasic dihydrate, pH 6.0, 30 %v/v PEG 300, 1 %v/v propylene glycol P400, 10 μM 15mPGD$_2$. The best crystals only diffracted to lower than 4 Å resolution at a synchrotron source. To improve resolution, we used the serial femtosecond crystallography.

Samples for serial femtosecond crystallography were prepared in 100 μl gas-tight syringes as previously described (3). Purified CRTH2 was reconstituted in LCP by mixing 2 parts of protein solution with 3 parts of LCP host lipids (monoolein/cholesterol/POPG = 9:1:1 by wt) using a syringe lipid mixer (2). For crystallization setup, each 100 μl syringe was filled with 20-50 μl of precipitant solution, into which 2-5 μl of protein-laden LCP was injected through a gauge 22 needle as an extended filament. All syringes were then sealed and placed in an incubator at 10 °C. After an overnight incubation at 10 °C, we observed that LCP in all syringes converted into a lamellar phase, which has high brightness under cross-polarized light, making it impossible to see if protein crystals are present. Therefore, the lipid mesophase was separated from the precipitant solution, consolidated together (~25 μl) and titrated with additional lipid (monoolein/cholesterol/POPG) in 1 μl increments until it converted back into LCP (2-5 μl total) and re-injected into new syringes filled with precipitant and incubated at 10°C. Crystals were observed after 2 d in the conditions containing 0.1 M sodium chloride, 0.1 M lithium sulphate, 0.1 M sodium citrate tribasic dihydrate, pH 6.0, 30 %v/v PEG 300, 1 %v/v propylene glycol P400, 10 μM 15mPGD$_2$. During sample transportation to XFEL, the LCP in all syringes converted into a sponge phase. The sponge phase with crystals was carefully separated from the precipitant and titrated with monoolein (~5 μl) and MAG 7.9 (~5 μl) to absorb the access of the precipitant and form an LCP (~50 μl final sample volume) for injection in the XFEL beam.

Diffraction data collection and structure determination. SFX data were collected at the CXI instrument (4) of the Linac Coherent Light Source (LCLS). LCLS operated at a wavelength of 1.33 Å (9.5 keV), delivering individual X-ray pulses of 35 fs duration with ~6×10^{11} photons per pulse focused into a spot size of approximately 1.5 μm in diameter using a pair of Kirkpatrick–Baez mirrors. Protein microcrystals of an average size of 5-10 μm (Fig S4) in LCP medium were injected into the XFEL beam focus region inside of a vacuum chamber using an LCP injector (5) with a 50 μm diameter nozzle at a sample flow rate of 0.44 μl min^{-1} . Single-shot diffraction patterns of randomly oriented crystals were

recorded at a rate of 7,200 patterns per minute (120 Hz) with a 2.3 megapixel Cornell–SLAC Pixel Array Detector CSPAD (6). The XFEL beam was attenuated to 12.4% (~7 × 10^{10} photons per pulse) of the full intensity to avoid detector saturation. A total of 850,000 images were recorded within ~2 hrs using ~50 μL of sample. 20,358 potential single-crystal diffraction patterns (crystal hits) were identified using Cheetah (7) with a threshold of 15 potential Bragg peaks. Indexing, integration and merging of the crystal diffraction data was performed using CrystFEL (8), which involved application of the indexing algorithms of MOSFLM (9), XDS (10) and DIRAX (11) followed by averaging and integration of Bragg peaks using a Monte Carlo integration algorithm (12). The final dataset that included diffraction data form 7,061 crystals was analysed by the STARANISO webserver (http://staraniso.globalphasing.org/cgi-bin/staraniso.cgi) and truncated to 3.2, 3.2, 2.6 Å resolution along the reciprocal unit cell vectors a*, b*, c*, respectively.

The structure was solved by the molecular replacement method with Phaser (13) using the previously published CRTH2 structure (PDB ID 6D27) as a model. Refinement was done by iterative cycling of automatic reciprocal space refinement with Phenix (14) and manual real-space adjustments using Coot (15). Final data collection and refinement statistics are shown in **Table 1**.

Radioligand binding assay and protein surface expression. The expression levels of wild type CRTH2 and mutants in Sf9 and HEK293 cells were determined by flow cytometry experiments. All constructs were expressed in Sf9 cells using the baculavirus system. After washing with PBS twice, cells were incubated with 1 μg/ml DyLight 488 (Thermo Fisher)-labeled anti-Flag M1 antibody (homemade) plus 2 mM $CaCl_2$ in dark for 15 min at room temperature. Staining of cells with DyLight 488-M1 antibody was analyzed by flow cytometry on a FACScan flow cytometer (BD CellQuestTM Pro). The protein expression levels were represented by the median fluorescence intensity of stained cells. Results were represented as the mean ± SEM from 3 independent measurements. All CRTH2 mutants could be expressed on the cell surface.

To prepare cell membranes for radioligand binding assays, cells expressing CRTH2 and mutants were resuspended and homogenized in buffer containing 20 mM Tris-HCl, pH 7.5, 1 mM EDTA, 0.2 μg/ml leupeptin and 100 μg/ml benzamidine. Then the samples were centrifuged at 500 g for 10 min to get the supernatant. The supernatant was centrifuged at 150,000 g for 40 min to pellet the membranes. The membrane pellet was resuspended in buffer containing 20 mM HEPES, pH7.5, 100 mM NaCl, 1 mM EDTA and homogenized with syringe, then frozen in liquid nitrogen and stored at -80°C for further use.

For the radioactive ^{3}H-PGD_2 saturation binding, ~20 μg of protein membrane was incubated with various concentrations of ^{3}H-PGD_2 (Perkin Elmer) from 0 to 15 nM in binding buffer containing 20 mM HEPES, pH 7.5, 1 mM EDTA, 5 mM $MgCl_2$, 5 mM $MnCl_2$ and 0.1% (w/v) BSA. Total and nonspecific binding were measured in the absence

and presence of 10 mM non-radioactive CAY10471 (Cayman Chemical), respectively. After 2h incubation at room temperature, the reaction was terminated by adding 4 mL of cold binding buffer and filtering through glass giber prefilters (Millipore Sigma). After 3 times wash with 4 mL cold binding buffer each, the retained receptor-bound ^{3}H-PGD$_2$ was incubated with 5 mL of CytoScint liquid scintillation cocktail (MP Biomedicals) and counted on a Beckman LS6500 scintillation counter. ^{3}H-PGD$_2$ saturation binding data were represented as the mean ± SEM from 3 independent experiments. Data were analyzed with the saturation binding methods in GraphPad Prism 7 (GraphPad Software).

Molecular Dynamics (MD) simulations. The CRTH2 protein was prepared for molecular dynamics (MD) simulations by first removing the 105-amino acid T4 lysozyme (mT4L) that was inserted into the receptor to promote crystallogenesis. The ICL3 region linking TM5 and TM6, along with the missing N-terminal residues 1-2 were modeled using MODELLER v 9.13 (16).

The N- and C- termini of the receptor were acetylated and amidated, respectively. Apo or holo configurations of CRTH2 (bound to 15mPGD$_2$) were then embedded into a TIP3P-solvated bilayer comprising 300 POPC (1-palmitoyl-2-oleoyl-s*n*-glycerol-3-phosphocholine) molecules using the *Membrane Builder* protocol as implemented in the CHARMM-GUI web server (17). The systems were neutralized by adding Na^+ and Cl^- ions at 150 mM concentration. The systems so prepared comprised ~126,000 atoms with dimensions ~107 Å x 107 Å x 119 Å. The protein, solvent, lipids and ions were modeled using CHARMM36 force field parameters (18). Initial parameters for the 15mPGD$_2$ molecule present in the holo simulations were generated using CHARMM general force field (CGenFF (19)) implemented through the ParamChem (20, 21) web server, which were further refined using the GAAMP (22) web server.

All simulations were performed using GROMACS v 5.1.2 (23). Long-range electrostatics was calculated with particle mesh Ewald (PME) scheme, while a 12 Å cut-off was employed for estimating short-range non-bonded interactions. The systems were first energy minimized, following which they were equilibrated by applying harmonic position restraints on non-solvent heavy atoms, which were gradually reduced over six equilibration steps. First, equilibration under an NVT ensemble was performed in three steps (50 ps each, 1 fs time-step) with the system temperature maintained at 303.15 K by Berendsen coupling. Subsequently, equilibration under an NPT ensemble maintained at 303.15 K and 1.0 bar using Berendsen coupling was performed in three steps (100 ps each, 2 fs time-step). H-atom containing bonds were constrained with LINCS algorithm (24). All restraints were removed post-equilibration and 1 μs-production runs were carried out at 303.15 K temperature (Nośe-Hoover thermostat) and 1.0 bar pressure (Parrinello-Rahman barostat). Pressure coupling was applied semi-isotropically during NPT equilibration steps and unrestrained production runs.

Analysis of MD simulation trajectories. Analysis tools available within the GROMACS v 5.1.2 suite such as *gmx rms*, *rmsf*, *distance*, *mindist*, *gyrate,* and *hbond*, along with in-house Perl scripts were used for analysis of the MD-generated trajectories. The distance and geometric criteria for identifying various non-covalent interactions have been adopted from Mishra *et al.* and references there in (25). The extraction of ligand translocation channels and calculation of their volumes in individual snapshots from the trajectories was carried out using the Channel Finder program from the 3V suite of programs (26).

References

1. T. S. Thorsen, R. Matt, W. I. Weis, B. K. Kobilka, Modified T4 Lysozyme Fusion Proteins Facilitate G Protein-Coupled Receptor Crystallogenesis. *Structure* **22**, 1657-1664 (2014).
2. M. Caffrey, V. Cherezov, Crystallizing membrane proteins using lipidic mesophases. *Nat Protoc* **4**, 706-731 (2009).
3. W. Liu, A. Ishchenko, V. Cherezov, Preparation of microcrystals in lipidic cubic phase for serial femtosecond crystallography. *Nat Protoc* **9**, 2123-2134 (2014).
4. S. Boutet, G. J. Williams, The Coherent X-ray Imaging (CXI) instrument at the Linac Coherent Light Source (LCLS). *New Journal of Physics* **12** (2010).
5. U. Weierstall *et al.*, Lipidic cubic phase injector facilitates membrane protein serial femtosecond crystallography. *Nature communications* **5**, 3309 (2014).
6. P. Hart *et al.* (2012) The CSPAD megapixel x-ray camera at LCLS. in *X-Ray free-electron lasers: beam diagnostics, beamline instrumentation, and applications* (International Society for Optics and Photonics), p 85040C.
7. A. Barty *et al.*, Cheetah: software for high-throughput reduction and analysis of serial femtosecond X-ray diffraction data. *Journal of applied crystallography* **47**, 1118-1131 (2014).
8. T. A. White *et al.*, Recent developments in CrystFEL. *Journal of applied crystallography* **49**, 680-689 (2016).
9. A. G. Leslie, The integration of macromolecular diffraction data. *Acta Crystallographica Section D: Biological Crystallography* **62**, 48-57 (2006).
10. W. Kabsch, Xds. *Acta Crystallographica Section D: Biological Crystallography* **66**, 125-132 (2010).
11. A. Duisenberg, DIRAX: a program for indexing twinned crystals. *J Appl Crystallogr* **25**, 92-96 (1992).
12. R. A. Kirian *et al.*, Structure-factor analysis of femtosecond microdiffraction patterns from protein nanocrystals. *Acta Crystallographica Section A: Foundations of Crystallography* **67**, 131-140 (2011).
13. A. J. McCoy *et al.*, Phaser crystallographic software. *J Appl Crystallogr* **40**, 658-674 (2007).
14. P. D. Adams *et al.*, PHENIX: a comprehensive Python-based system for macromolecular structure solution. *Acta Crystallogr D Biol Crystallogr* **66**, 213-221 (2010).
15. P. Emsley, K. Cowtan, Coot: model-building tools for molecular graphics. *Acta Crystallogr D Biol Crystallogr* **60**, 2126-2132 (2004).

16. A. Šali, T. L. Blundell, Comparative protein modelling by satisfaction of spatial restraints. *Journal of molecular biology* **234**, 779-815 (1993).
17. S. Jo, T. Kim, V. G. Iyer, W. Im, CHARMM-GUI: a web-based graphical user interface for CHARMM. *Journal of computational chemistry* **29**, 1859-1865 (2008).
18. J. B. Klauda *et al.*, Update of the CHARMM all-atom additive force field for lipids: validation on six lipid types. *The journal of physical chemistry B* **114**, 7830-7843 (2010).
19. K. Vanommeslaeghe *et al.*, CHARMM general force field: A force field for drug-like molecules compatible with the CHARMM all-atom additive biological force fields. *Journal of computational chemistry* **31**, 671-690 (2010).
20. K. Vanommeslaeghe, A. D. MacKerell Jr, Automation of the CHARMM General Force Field (CGenFF) I: bond perception and atom typing. *Journal of chemical information and modeling* **52**, 3144-3154 (2012).
21. K. Vanommeslaeghe, E. P. Raman, A. D. MacKerell Jr, Automation of the CHARMM General Force Field (CGenFF) II: assignment of bonded parameters and partial atomic charges. *Journal of chemical information and modeling* **52**, 3155-3168 (2012).
22. L. Huang, B. Roux, Automated force field parameterization for nonpolarizable and polarizable atomic models based on ab initio target data. *Journal of chemical theory and computation* **9**, 3543-3556 (2013).
23. M. J. Abraham *et al.*, GROMACS: High performance molecular simulations through multi-level parallelism from laptops to supercomputers. *SoftwareX* **1**, 19-25 (2015).
24. B. Hess, H. Bekker, H. J. Berendsen, J. G. Fraaije, LINCS: a linear constraint solver for molecular simulations. *Journal of computational chemistry* **18**, 1463-1472 (1997).
25. N. K. Mishra, R. Krishna Deepak, R. Sankararamakrishnan, S. Verma, Controlling in vitro insulin amyloidosis with stable peptide conjugates: A combined experimental and computational study. *The Journal of Physical Chemistry B* **119**, 15395-15406 (2015).
26. N. R. Voss, M. Gerstein, 3V: cavity, channel and cleft volume calculator and extractor. *Nucleic acids research* **38**, W555-W562 (2010).

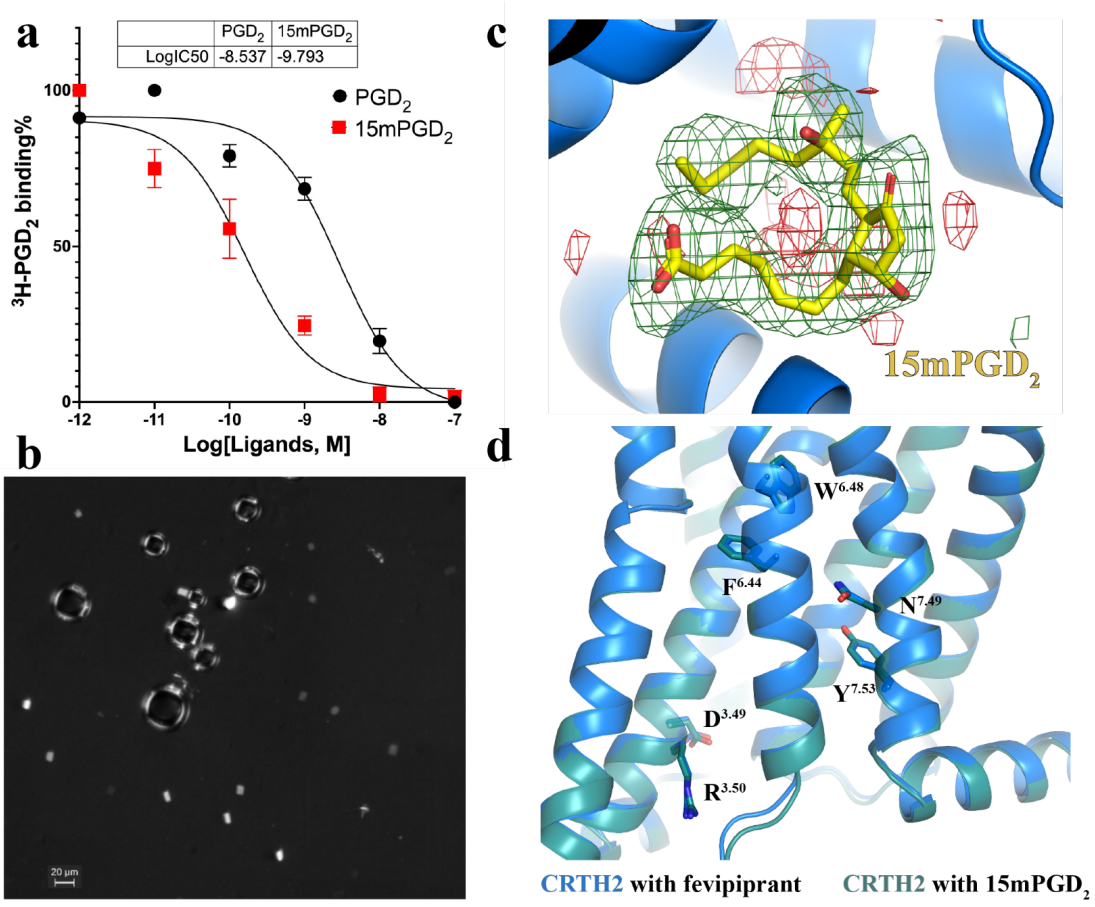

Figure S1. $15mPGD_2$ binding, crystals of CRTH2-$15mPGD_2$ and structural comparison of CRTH2 with fevipiprant and with $15mPGD_2$. (a) Competition binding of PGD_2 and $15mPGD_2$ on CRTH2 using ^{3}H-PGD_2 as the radioligand. HEK293 cell membranes overexpressing wtCRTH2 were prepared and used in the binding assays. Each data point in the left panel was shown as mean ± SEM. n=3. **(b)** Crystals of CRTH2-$15mPGD_2$ grown in lipidic cubic phase for structure determination by serial femtosecond crystallography. The picture was taken under a stereo microscope using cross-polarizers. **(c)** mF_o-DF_c simulated annealing ligand omit electron-density map for $15mPGD_2$ contoured at 3.0 σ shown as green (positive) / red (negative) mesh. $15mPGD_2$ is shown as sticks with yellow carbons. **(d)** Structural alignment of conserved residues in the structures of CRTH2 bound to fevipiprant (PDB ID) and $15mPGD_2$. The CRTH2 residues shown as sticks are D128$^{3.49}$ and R129$^{3.50}$ from the DR$^{3.50}$Y/F/C motif, W259$^{6.48}$ and F255$^{6.44}$ from the FxxCW$^{6.48}$xP motif, and N300$^{7.49}$ and Y304$^{7.53}$ from the NP$^{7.50}$xxY motif. All three motifs are highly conserved in class A GPCRs, which undergo conformational changes during receptor activation.

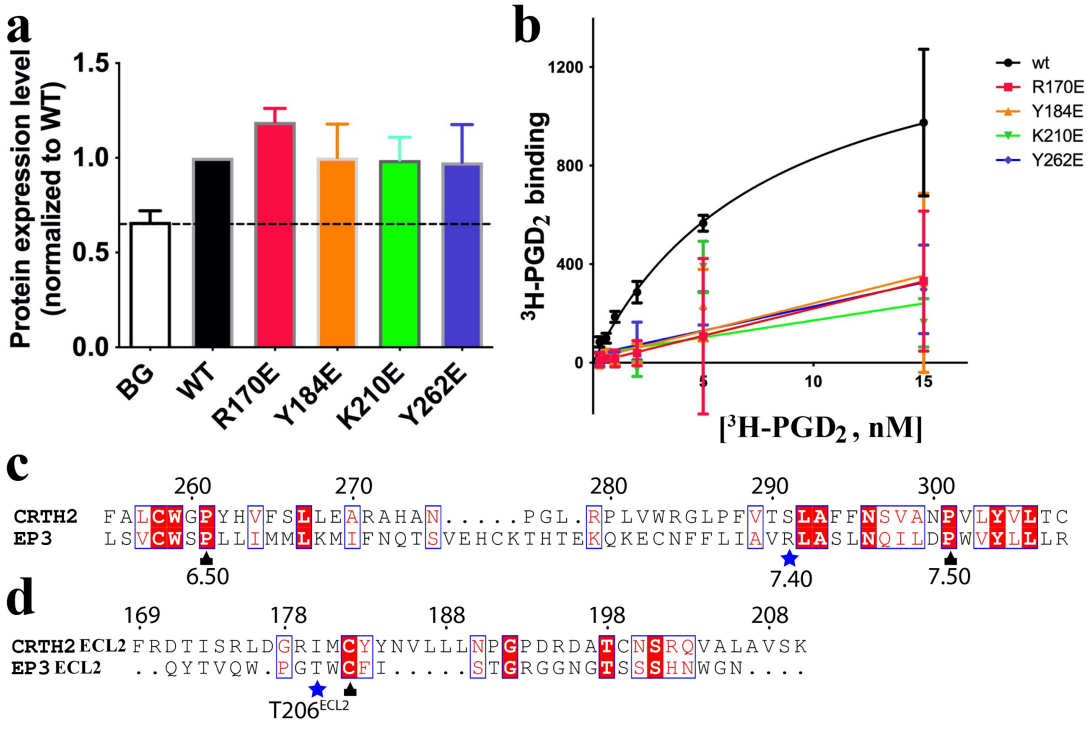

Figure. S2: Charge-switching mutations and Sequence alignment of CRTH2 and EP3. (**a**) Expression levels of CRHT2 (WT) and mutants with charge-switching mutations R170E, Y184E, K210E and Y262E in HEK293 cells determined by fluorescent antibody staining. **(b)** Saturation binding assays on different CRTH2 constructs using ^{3}H-PGD$_2$. All CRTH2 constructs were transiently expressed in HEK293 cells and cell membranes were prepared and used in the ligand-binding assays. No saturable ^{3}H-PGD$_2$ binding was observed for all four mutants. Each data point in the left panel was shown as mean ± SEM. n=3. (**c**) Alignment of the segments of TM6 and TM7 in CRTH2 and EP3. Black arrows indicate conserved P$^{6.50}$ and P$^{7.50}$ residues. The blue star points to the non-conserved 7.40 residues in CRTH2 and EP3. (**d**) Alignment of ECL2s in CRTH2 and EP3. The black arrow points to the conserved C^{ECL2} residues in both receptors that form disulfide bonds. The blue star points to T206^{ECL2} in EP3, which is an Ile residue in CRTH2.

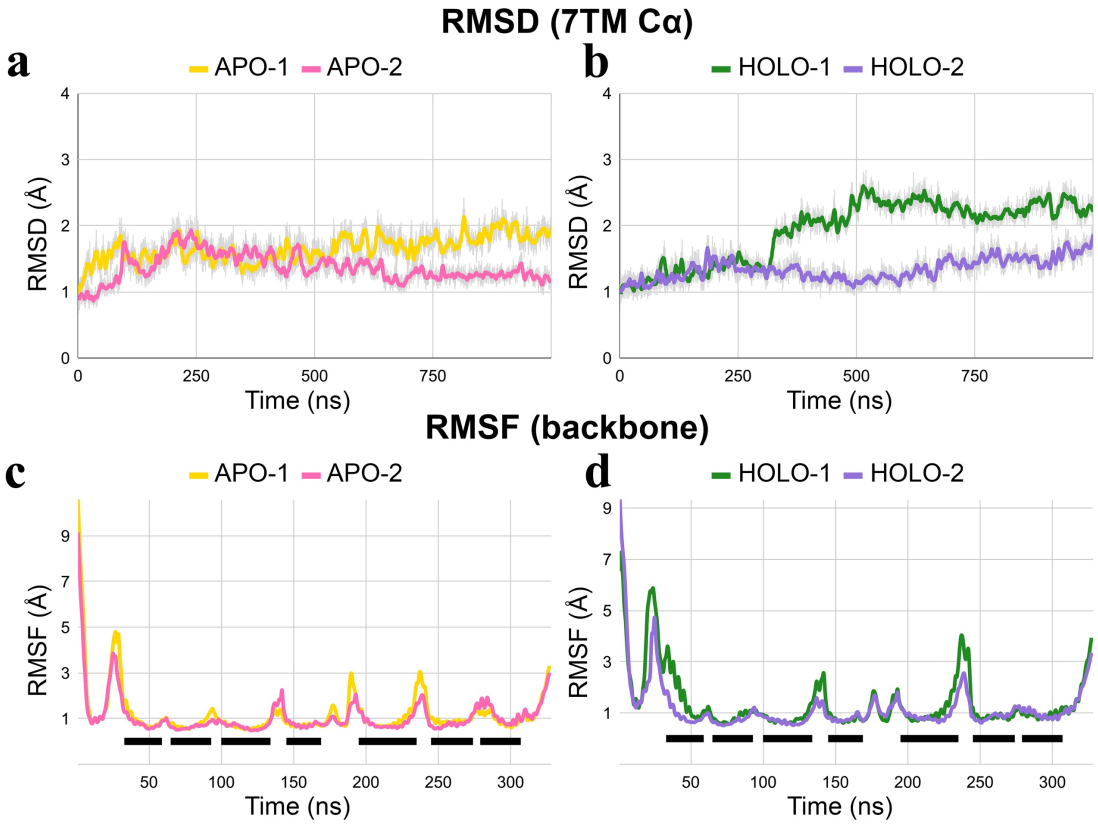

Figure. S3. RMSD and RMSF curves in four CRTH2 MD simulation systems. (a) RMSD (root-mean-square deviation) of the Cα of 7-TMs in apo-1 (yellow) and apo-2 (pink). **(b)** RMSD of the Cα of 7-TMs in holo-1 (green) and holo-2 (purple). **(c)** RMSF (root-mean-square fluctuation**)** of all the protein backbone atoms in apo-1 (yellow) and apo-2 (pink). **(d)** RMSF of all the protein backbone atoms in holo-1 (green) and holo-2 (purple). In **c** and **d**, the regions corresponding to the 7-TMs (seven transmembrane helices) of CRTH2 are shown as horizontal black bars. The values in **a-d** are calculated using the equilibrated starting structure of CRTH2 (t = 0 ns) as the reference.

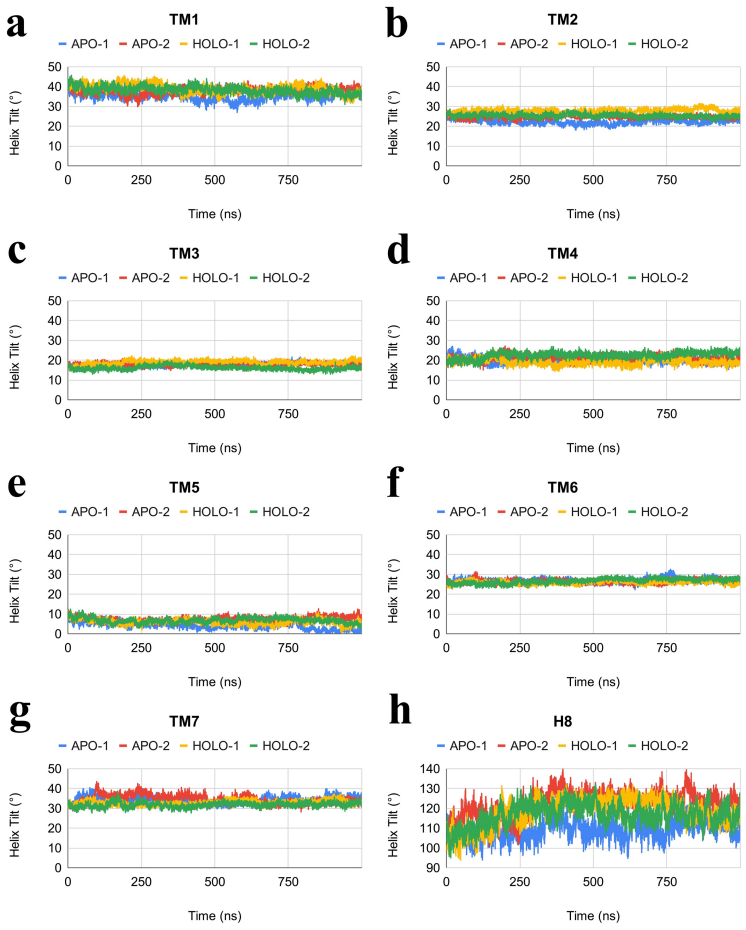

Figure. S4. Evolution of tilt angles of TM1-7 (a-g) and helix 8 (H8) (h) in all four systems. The tilt angle is calculated using the *gmx* bundle by measuring the angle subtended by the helix axis with the normal to the plane of the membrane.

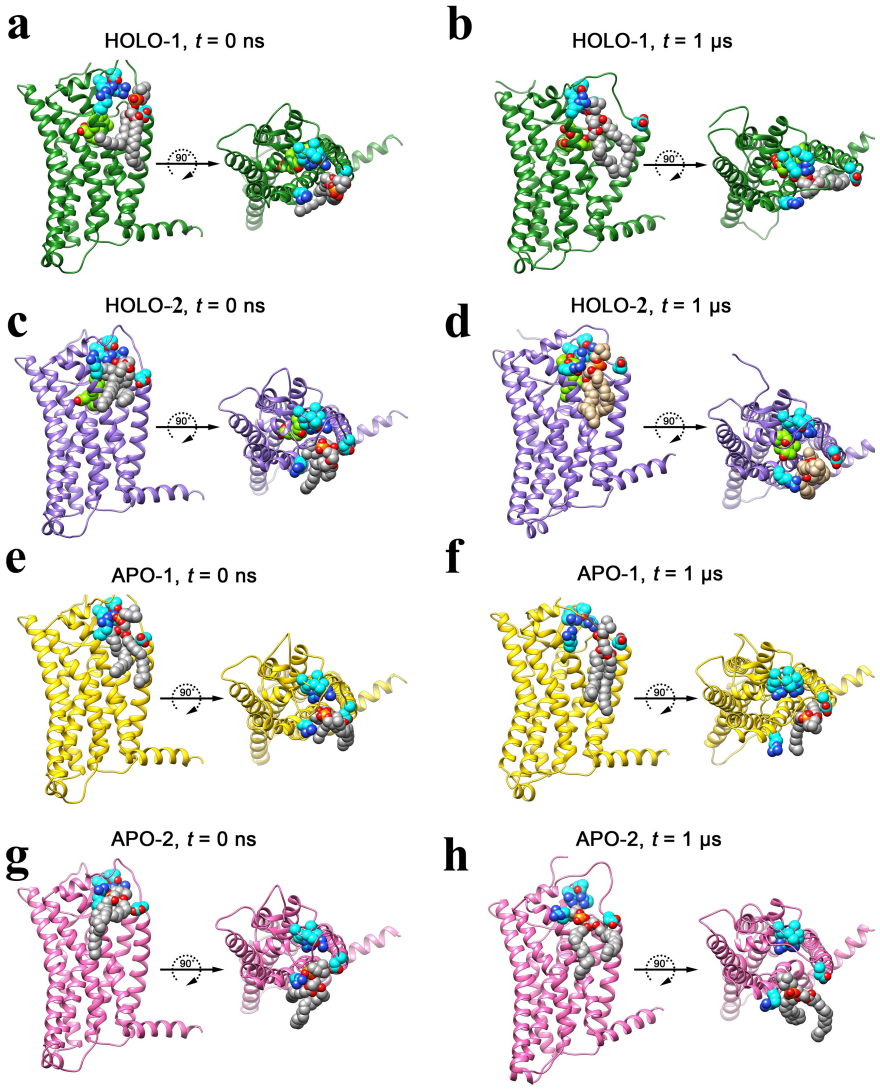

Figure. S5. Positions of POPC molecules near the TM1-TM7 cleft in all simulations. Position of POPC molecules near the TM1-TM7 cleft at t = 0 ns in **a)** holo-1, **c)** holo-2, **e)** apo-1, **g)** apo-2, and at t = 1 µs in **b)** holo-1, **d)** holo-2, **f)** apo-1, and **h)** apo-2. All displayed atoms are in sphere representation. The entry port residues, viz., $D32^{1.32}$, $R284^{7.32}$, $H95^{ECL1}$, $R175^{ECL2}$, $D177^{ECL2}$ and $R179^{ECL2}$, are in cyan, the POPC molecules are in grey, and the bound 15mPGD$_2$ molecule (holo) is in light green. The POPC molecule in **d** is shown in tan as it is a different molecule compared to the one in **c**.

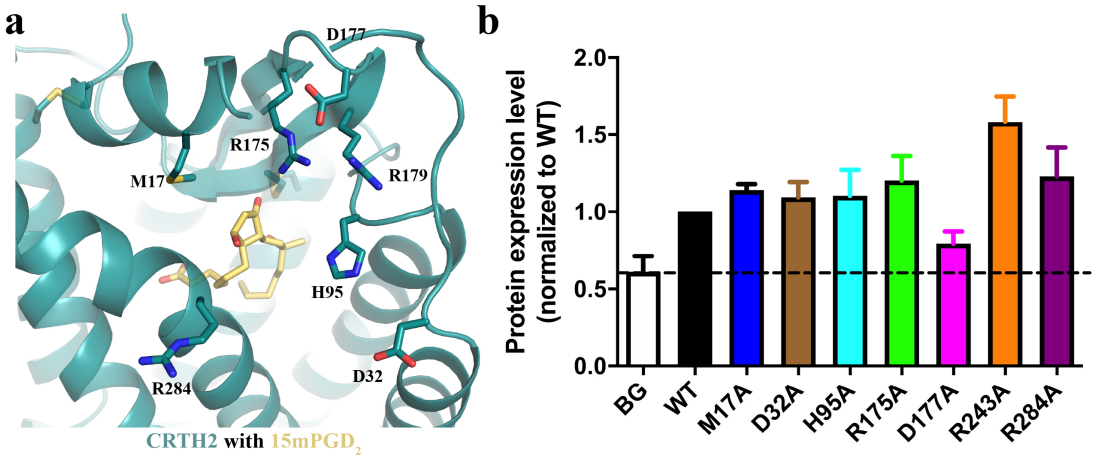

Figure. S6. CRTH2 mutations and expression. (**a**) Residues at the ligand entry port of CRTH2. The ligand 15mPGD$_2$ is shown as yellow sticks. **(b**) Expression levels of CRHT2 and mutants in the main Figure 5d in Sf9 cells determined by fluorescent antibody staining. **T**he results were from 3 independent assays and the data are shown as mean ± s.e.m..

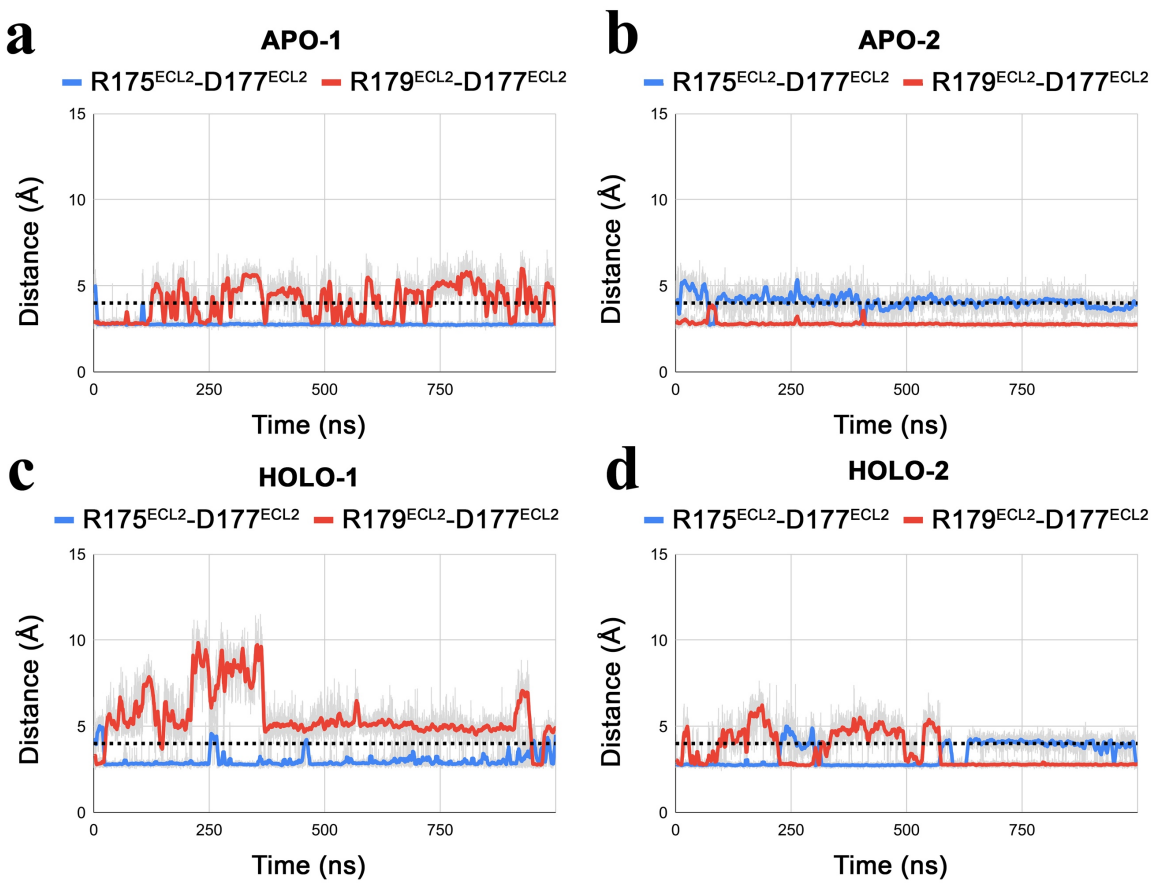

Figure. S7. Evolution of R175^{ECL2}-D177^{ECL2} and R179^{ECL2}-D177^{ECL2} salt bridges in MD simulations. Evolution of R175^{ECL2}-D177^{ECL2} (red) and R179^{ECL2}-D177^{ECL2} (blue) salt-bridges in **a)** apo-1, **b)** apo-2, **c)** holo-1, and **d)** holo-2. The dotted line denotes the cut-off distance of 4.0 Å used to define salt-bridge interactions.

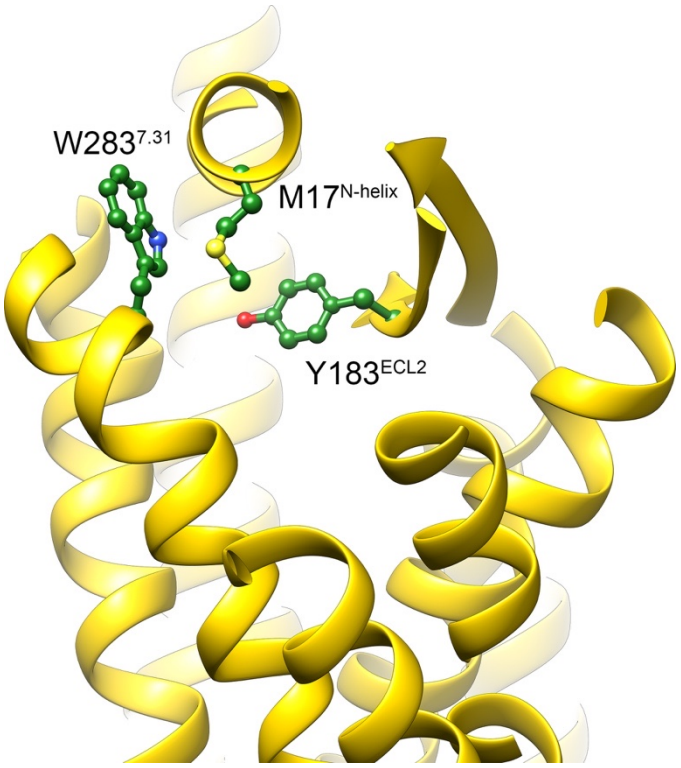

Figure. S8. Positions of W283$^{7.31}$, M17$^{N\text{-helix}}$ and Y183^{ECL2} in the structure. Arrangement of residues W283$^{7.31}$, M17$^{N\text{-helix}}$ and Y183^{ECL2} forming the "Aro-Met-Aro" bridging motif observed in the CRTH2 crystal structure.

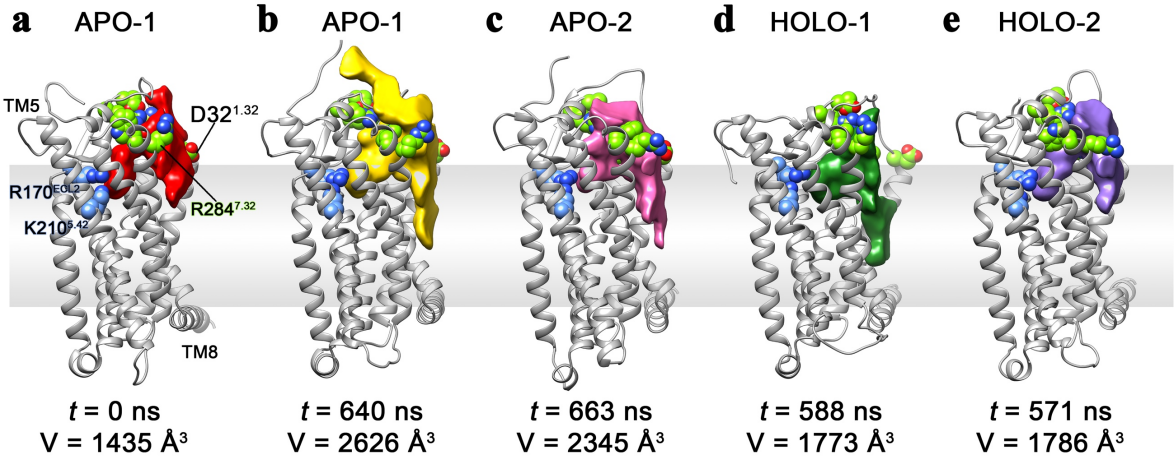

Figure. S9. Potential ligand translocation channel. Ligand translocation channels (surface representation) extracted from representative CRTH2 structures from MD simulations of **a)** apo-1 at t = 0 ns (red), **b)** apo-1 at t = 640 ns (yellow), **c)** apo-2 at t = 663 ns (pink), **d)** holo-1 at t = 588 ns (green), and **E)** holo-2 at t = 571 ns (purple). The channels are extracted using the Channel Finder program of the 3V suite of programs. Small and large probe radii of 2.0 Å and 12.5 Å, respectively, were used for identifying the channels. The positions of the binding site residues R170^{ECL2} and K210$^{5.42}$ (blue) are shown in sphere representation. The residues lining the entry port (light green) are shown in sphere representation with the positions of D32$^{1.32}$ and R284$^{7.32}$ indicated using labels in **a**. The position of TM5 and TM8 are also indicated in **a** for reference.

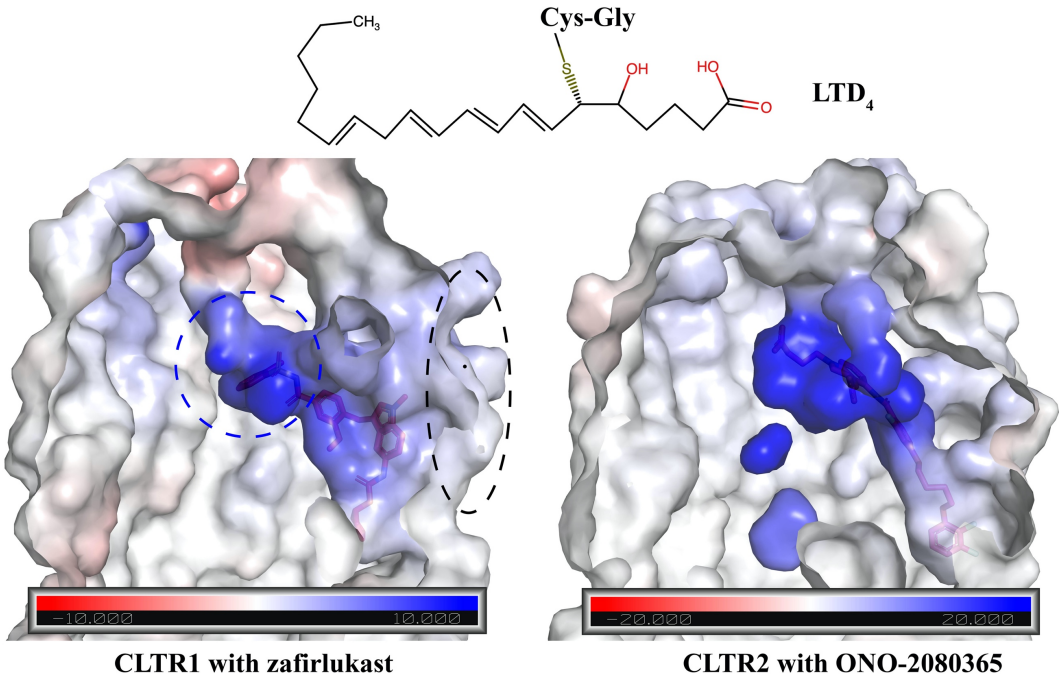

Figure. S10. Uneven positive charge distribution of the ligand-binding pockets in CLTRs. The positively charged ligand-binding pockets in the crystal structures of CLTR1 with the antagonist zafirlukast (PDB ID 6RZ5) and CLTR2 with the antagonist ONO-2080365 (PDB ID 6RZ8) are shown in the figure. The charge distribution was calculated by APBS Electrostatics (https://www.cgl.ucsf.edu/chimera/docs/ContributedSoftware/apbs/apbs.html). The antagonists are shown as sticks. The chemical structure of LTD_4 is shown on the top of the figure. The lateral lipid entrance and the potential binding site for the carboxylate of LTD_4 in CLTR1 are shown with black and blue circles, respectively.